

# Microstructures and mechanical properties of Ti6Al4V-Ti48Al2Cr2Nb alloys fabricated by laser melting deposition of powder mixtures

Ruixin Ma<sup>a</sup>, Zhanqi Liu<sup>a</sup>, Wenbo Wang<sup>a</sup>, Guojian Xu<sup>a,\*</sup>, Wei Wang<sup>b</sup>

<sup>a</sup> School of Material Science and Engineering, Shenyang University of Technology, Shenyang 110870, China

<sup>b</sup> School of Mechanical Engineering, Shenyang University of Technology, Shenyang 110870, China



## ARTICLE INFO

### Keywords:

Laser melting deposition  
Ti6Al4V  
Ti48Al2Cr2Nb  
Microstructure  
Phase transformation  
Tensile properties

## ABSTRACT

Ti6Al4V (TC4)/Ti48Al2Cr2Nb (TiAl) functionally graded materials (FGM) is the premium material for aero-engine turbine blisk in which TC4 and TiAl were used as blades and disks, respectively, and has wide application prospect. In this work, TC4-*x*TiAl (*x* = 20%, 40%, 60%, 80% wt%) alloys without metallurgical defects were fabricated by laser melting deposition (LMD) from mixtures of TC4/TiAl powders. The influence of TiAl content on microstructure morphology, phase composition, and tensile properties was systematically studied in detail and a composition-microstructure-property relationship was simultaneously set up. The microstructure gradually transformed from basket weave structure to lamellar structure, accompanying with the formation of  $\alpha_2$ ,  $\gamma$ , and B2 with increasing TiAl contents. In addition, a series of phase transformations occurred in these alloys:  $\beta \rightarrow \alpha$ ,  $\alpha \rightarrow \alpha_2$ , and  $\alpha_2 \rightarrow \gamma$ . The addition of TiAl can reduce the tensile properties at room temperature (RT), the TC4-20%TiAl alloy has the highest ultimate tensile strength (UTS) (1083 MPa) and elongation (4.60%). Compared to other alloys, the TC4-60%TiAl alloy exhibited the best tensile property at 650 °C and 750 °C, the UTS of which was 572 MPa and 562 MPa, respectively. The tensile properties at RT and high-temperature are strongly dependent on phase composition. The formation of  $\alpha_2$  and  $\gamma$  intermetallic compounds can improve the thermal stability, but reduce the room-temperature strength and plasticity. In particular, the  $\gamma$  phase is more stable than the  $\alpha_2$  phase at high temperatures.

## 1. Introduction

Laser melting deposition (LMD) is a very common laser additive manufacturing (LAM) method capable to fabricate near net-shape metallic components with complex shapes and sizes directly from computer-aided design (CAD) models [1,2]. During LMD, a laser beam guided by an optical system forms a molten pool on the substrate, at the same time the metal powders are transported to the molten pool by the powder feeder under the inert atmosphere, then completely melt and rapidly solidify. By LMD software, the laser head and the workbench move along the pre-designed path. Thus, the three-dimensional components can be stacked in layers without mold manufacturing [3,4]. LMD has become an important approach to build functionally graded material (FGM) and multi-material composite structures (MMCS) due to the flexibility in controlling material composition, solidification structure, and external dimensions [5,6].

TC4 titanium alloy (Ti-6Al-4V) is the typical ( $\alpha$  +  $\beta$ ) dual-phase titanium alloy, which can work stably below 500 °C [7,8], and is widely used in aerospace engineering with the characteristics of high specific

strength, well corrosion resistance and heat resistance [9–11]. Compared with the traditional single TC4 structure, the FGM integrally formed on the basis of TC4 parts can not only reduce component weight but also improve other properties, which meets the requirements of lightweight and high performance in the aerospace field [12,13]. Since the 1950s, material scientists have studied the TiAl alloys as a lightweight substitute for nickel-based superalloys due to their characteristics of excellent high-temperature antioxidative properties, high melting points (1460 °C), low density (3.9–4.2 g/cm<sup>3</sup>), high elastic modulus (160–180 GPa), and high operating temperature (700–900 °C) [14,15]. Accordingly, FGM of TC4/TiAl can offer a unique combination of the TC4 (operating temperature  $\leq$  500 °C) and the TiAl (operating temperature  $\leq$  900 °C). Thus, studying these structures is crucial to the development of new materials in aerospace engineering.

In recent years, several FGM (such as Ti/TiAl, Ti/Ti-6Al-2Zr-1Mo-1V, TA2/Ti-6.5Al-2Zr-1Mo-1V Ti/Ti-6Al-4V, TA15/Inconel 718, and  $\gamma$ -TiAl/Ti<sub>2</sub>AlNb) have been fabricated by LMD and became popular, their compositions, microstructure evolution, and overall properties were analyzed [12,16–20]. However, brittle phases, which are in the

\* Corresponding author.

E-mail address: [xuguojian@sut.edu.cn](mailto:xuguojian@sut.edu.cn) (G. Xu).

interfacial transition zone of FGM reduce the transition zone performance and cause cracks [21,22]. Moreover, due to the significant difference in thermal expansion coefficients (TEC) between TC4 and TiAl, the transition zone of TC4/TiAl bimetallic structure is usually the weakest part [23,24]. Analysis of the microstructure evolution of the different ratios of TC4 and TiAl powders is necessary to understand the interface fracture mechanism of the FGM, it will help to inhibit brittle phase formation, fabricate FGM and improve the performance of component in high-temperatures ( $> 600^{\circ}\text{C}$ ) [25,26].

As a consequence, from the perspective of TC4/TiAl FGM design, it is valuable to research the microstructure and properties of TC4-TiAl alloys fabricated by LMD. In the present paper, we fabricated specimens of the TC4-20%TiAl, TC4-40%TiAl, TC4-60%TiAl, TC4-80%TiAl alloys by LMD. The study focus on corresponding microstructures, phase evolutions, and their contributions to the tensile properties at room-temperature (RT) and high-temperature ( $650^{\circ}\text{C}$  and  $750^{\circ}\text{C}$ ). A relationship of composition-microstructure-property was established through observation using SEM, EBSD, and TEM. This present study lays a theoretical foundation for the further study of TC4/TiAl FGM, of which the powder compositions from TC4 side to TiAl side are 100%TC4, TC4-20%TiAl, TC4-40%TiAl, TC4-60%TiAl, TC4-80%TiAl and 100%TiAl.

## 2. Materials and methods

### 2.1. Materials

The TC4 (Ti-6Al-4V) powder, with particle diameters in the 75–250  $\mu\text{m}$  range was purchased from Baoji Haibao Special Metals Materials Co., Ltd. (China). TiAl powder (with nominal composition expresses as Ti-48Al-2Cr-2Nb) with particle diameters in the 53–150  $\mu\text{m}$  range was provided by Beijing AMC Powders Metallurgy Technology Co., Ltd. (China). Both powders were prepared by vacuum atomization methods. The LMD specimens of TC4-20%TiAl (wt%), TC4-40%TiAl (wt%), TC4-60%TiAl (wt%), and TC4-80%TiAl (wt%) were denoted as specimen 1, specimen 2, specimen 3, and specimen 4, respectively (see Fig. 1(a-d)). Prior to LMD, powders were mixed for 4 h and then dried at  $150^{\circ}\text{C}$  for 2 h in a vacuum furnace. A TC4 plate with a

**Table 1**

The chemical composition of the Ti6Al4V powder, Ti48Al2Cr2Nb powder, and Ti6Al4V substrate used (wt%).

Elements	Ti6Al4V powder/substrate	Elements	Ti48Al2Cr2Nb powder
Al	6.02	Al	32.5
V	3.82	Nb	4.62
O	0.16	Cr	2.64
N	0.03	O	0.16
Ti	Bal.	Ti	Bal.

dimension of  $100 \times 50 \times 10$  mm was used as a substrate. The chemical composition of the Ti6Al4V powder, Ti48Al2Cr2Nb powder, and Ti6Al4V substrate used in this paper are shown in Table 1. Before deposition, the surface of TC4 plate was polished and wiped with acetone to remove the oxide layers from the substrate.

### 2.2. Experimental equipment

LMD8060 system used as the experimental equipment in this study was provided by Nanjing Zhongke Raycham Laser Technology Co., Ltd. (China), and it is consisted of an LDF-4000 fiber-coupled diode laser system, a three-axis linkage CNC table, a four-way powder feeding 3D printing head, a gas-borne powder feeder, a cooler and a sealed chamber. Argon with a purity  $> 99.9994\%$ , was used as the carrier gas for powder feeding and shielding gas in the sealed chamber to prevent the molten pool from oxidizing. At the same time, the oxygen and steam level in the sealed chamber is strictly controlled to be lower than 50 ppm to ensure the chemical composition and mechanical properties of specimens. Subsequent tests proved that these gas elements had no effect on the experimental results. The flow rate of argon for powder feeding was optimized through experiments. In the current work, the argon flow rate of 7 l/min as powder feeding was employed to ensure the stable powder flow during LMD. The following LMD processing parameters were selected: 1900 W laser power, 420 mm/min scanning speed, 4.96 g/min powder delivery rate, 3 mm focal diameter, 0 mm defocusing distance and about 0.8 mm average layer thickness.

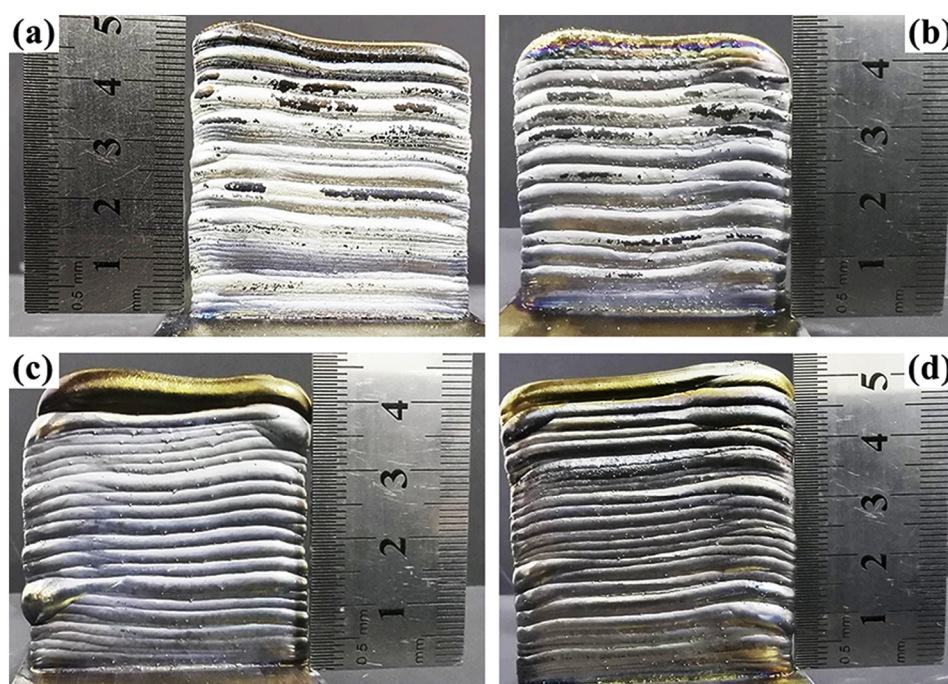


**Fig. 1.** LMD thin-walled specimens of TC4-TiAl alloys: (a) specimen 1; (b) specimen 2; (c) specimen 3; (d) specimen 4.

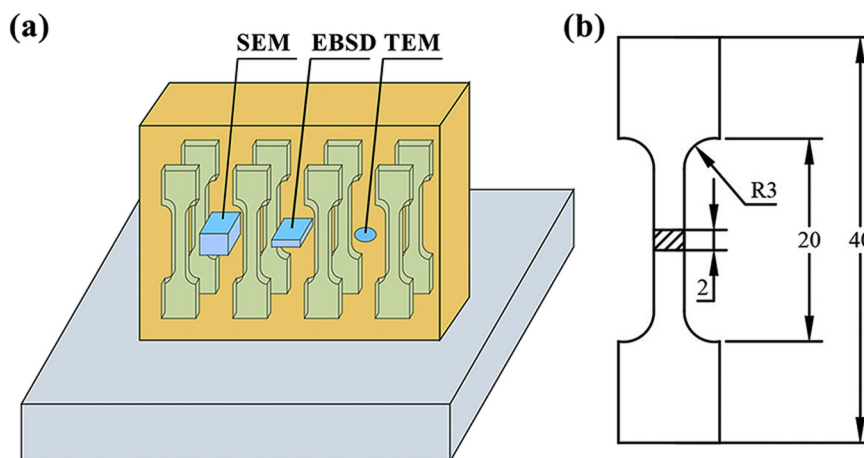


**Fig. 2.** Sampling position, geometry and dimension of SEM samples, EBSD samples, and TEM samples, and tensile samples: (a) Sampling position of SEM samples, EBSD samples, and TEM samples; (b) Geometry and dimension (mm) of the tensile samples.

### 2.3. Microstructural and mechanical property characterization

After LMD, thin-walled specimens were sectioned into pieces using electric discharge for analyzing. Sampling position of SEM samples, EBSD samples, and TEM samples are shown in Fig. 2(a). Specimens were first ground to 3000 mesh using SiC abrasive paper and then mechanically polished. Then the SEM samples were etched using Kroll's reagent (containing 60 ml of distilled water, 6 ml of HNO<sub>3</sub>, and 1 ml of HF) for 5–30 s. EBSD samples were electro-polished in a solution of 6% perchloric acid, 34% butanol and 60% methanol by volume at –20 °C. TEM samples were obtained by twin-jet electronic polishing with the same electrolyte as that of EBSD.

The microstructures of the as-deposited LMD specimens were observed using the back-scattered electron (BSE) mode on a ZEISS GeminiSEM 300 scanning electron microscope (SEM) and JEM-2100 transmission electron microscope (TEM). Fracture morphology was characterized by S-3400 SEM. The electron backscattered diffraction (EBSD) performed with a step size of 0.4 μm was implemented to determine phase distributions by adopting a ZEISS GeminiSEM 300 SEM. Then the HKL Channel 5 analysis software was used to manipulate the EBSD data. Chemical compositions were determined by using X-ray fluorescence (XRF) spectroscopy. Tensile properties at room and high (650 °C and 750 °C) temperatures were tested on the WDW-100 system at a tensile rate equal to 0.5 mm/min. Geometry and dimension of the tensile samples for measurements of tensile strength are given in Fig. 2(b).

## 3. Results and discussion

### 3.1. Microstructure morphology

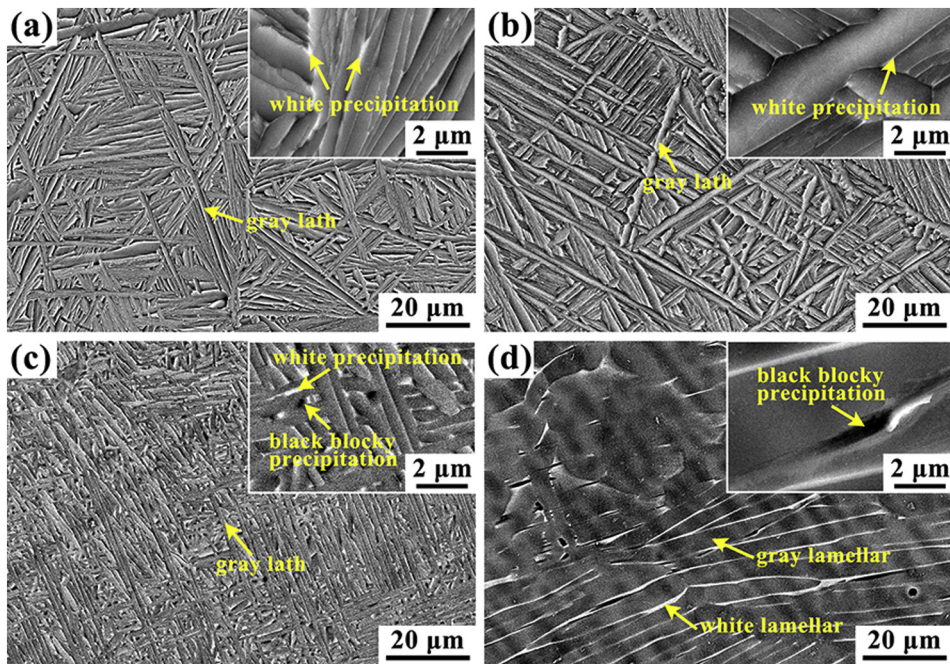
Fig. 3 shows SEM backscattered microstructures of the as-deposited LMD specimens. The microstructures transformed from basketweave structure (Fig. 3(a)–(c)) to lamellar structure (Fig. 3(d)) with increasing TiAl contents. As shown in Fig. 3, the microstructures of the alloys with different powder mixtures were composed of gray lath-like or lamellar-like matrix embedded with the minor patchy white precipitated phase and black block precipitate phase at the sub-boundaries of matrix phases, which were significantly different from the microstructure of the as-deposited pure TC4 and TiAl alloys [9,14]. According to Fig. 3(a)–(b), the gray lath-like matrix morphology of specimen 1 and specimen 2 basically resembled. However, the coarsening of gray laths of specimen 2 occurred clearly compared with that of the microstructure of specimen 1. The images in the insets of Fig. 3(a)–(b) shown microstructural details between gray laths. It is observed from Fig. 3(a)–(b) that a few white precipitations remained between adjacent

gray laths. Compared with specimen 1 and specimen 2, the gray laths shown in Fig. 3(c) were clearly refined, accompanying with the black blocky precipitations and white precipitations between gray laths from the inset image of Fig. 3(d). As revealed in Fig. 3(d), when the content of TiAl increased to 80%, the microstructure of specimen 4 consisted of gray lamellar-like matrix, occurring with the white lamellar precipitations and a little bit of black blocky precipitations dotting on gray lamellar boundaries, which can be observed in the TiAl alloy parts fabricated by LMD commonly [22]. The black precipitated phases enriched in Al, while the white precipitated phases were rich in Nb, V, and Cr, which was attributed to the fact that inhomogeneous distributions of elements during deposition gave rise to microsegregation [27].

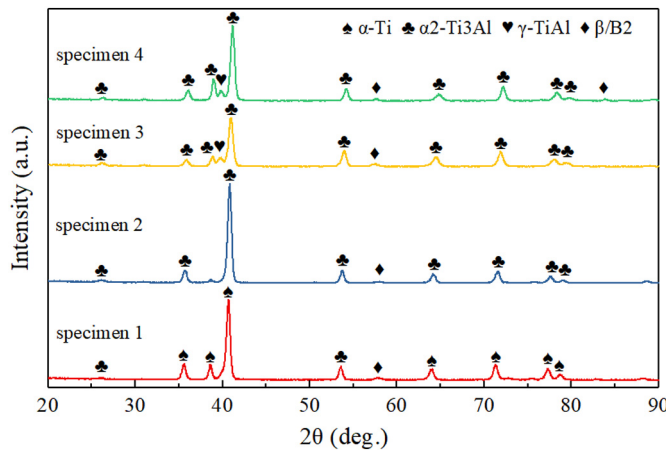
### 3.2. Phase composition

Fig. 4 shows the XRD pattern obtained on the as-deposited TC4-TiAl alloys. It revealed that the phase compositions of specimen 1, specimen 2, specimen 3 and specimen 4 are α-Ti + α<sub>2</sub>-Ti<sub>3</sub>Al + β/B2, α<sub>2</sub>-Ti<sub>3</sub>Al + β/B2, α<sub>2</sub>-Ti<sub>3</sub>Al + γ-TiAl + β/B2, and α<sub>2</sub>-Ti<sub>3</sub>Al + γ-TiAl + β/B2, respectively. When the TiAl content increased from 20% to 40%, solid solution α-Ti(α) changed into α<sub>2</sub>-Ti<sub>3</sub>Al(α<sub>2</sub>) by ordering transformation because of the increasing Al content in the specimen 2. As the TiAl content is > 60%, the diffraction peak of γ-TiAl(γ) could be observed obviously but cannot be seen in the specimen 1 and specimen 2. As increased to 80% TiAl, the weak diffraction peak located in 83.8° signified the formation of a few β/B2.

Further investigation was conducted on the LMD-produced alloys with different powder mixtures to characterize the microstructure and quantify the phase content using EBSD. Fig. 5 illustrates the combination of phase distributions and band contrast of transverse cross-section of four alloys, the black lines in which indicate laths or lamellar boundaries identified by EBSD. According to the result of Fig. 5, as TiAl content increased from 20% to 40%, the α changed to the α<sub>2</sub> by ordering transformation and disappeared completely in specimen 2. The microstructures of specimen 1 were consist of α (57.2%), α<sub>2</sub> (42.6%) and β/B2 (0.2%), while the microstructures of specimen 2 were consist of α<sub>2</sub> (99.9%) and β/B2 (0.1%). Meanwhile, the β/B2 contents of specimen 1 and specimen 2 were very low, being 0.2% and 0.1%, which possibly cannot be identified totally due to its small size. As the content of TiAl increased to 60%, it could be observed that blocky γ and β/B2 with a ratio of 2.92% and 1.38%, respectively, were discontinuously precipitated at the lath boundaries of α<sub>2</sub>. Precipitated phases are more conducive to formation at the boundaries due to lower interfacial energy compared to other areas [28]. As shown in Fig. 5(d), β/B2 (2.01%) and γ (1.09%) phases between α<sub>2</sub> (96.9%) lamellar precipitated and the β/B2 phases further elongated along the α<sub>2</sub> lamellar boundaries.



**Fig. 3.** Backscattered electron images of microstructure morphology of the as-deposited LMD alloys: (a) specimen 1; (b) specimen 2; (c) specimen 3; (d) specimen 4.



**Fig. 4.** XRD patterns of as-deposited LMD alloys.

Furthermore, the  $\gamma$  phase and the  $\beta/B2$  phase in specimen 3 which were small in size and uniformly distributed between the  $\alpha_2$  laths had the effect of dispersion strengthening. In contrast, the  $\gamma$  phase and the  $\beta/B2$  phase in specimen 4 had obvious aggregated and grew. Based on the analysis above, the gray phase, the white phase, and the black phase shown in Fig. 3 represented to the  $\alpha/\alpha_2$ ,  $\beta/B2$ , and  $\gamma$  respectively.

### 3.3. Phase transformation

Undoubtedly, the microstructures have an extremely effect on mechanical properties of alloys, and it is quite essential to reveal the mechanism of microstructure formation and the reaction behaviors of different elements during the LMD. Ti-Al phase diagram shown in Fig. 6 (in which composition range of specimen 1, specimen 2, specimen 3, and specimen 4 separately labeled by 1, 2, 3, and 4 gray areas) can provide information on phase transitions occurring with the alloys during cooling. Thus, the solidification behavior of the specimens during cooling can be determined. Actually, the allotropic transformation from  $\beta$  to  $\alpha$  firstly took place at high-temperature. Transformations of  $\beta$  (BCC) to  $\alpha$  (HCP) generally satisfies the

orientation relationship. Because of the characteristics of the cubic and hexagonal symmetries, 12 different crystalline orientation  $\alpha$  (which are often called 12  $\alpha$  variants) can nucleate in the  $\beta$  matrix [29]. According to Fig. 7(a), the decomposition of  $\beta$  among  $\alpha$  could be found, which revealed the existence of  $\beta \rightarrow \alpha$  phase transformation during cooling. Based on the measured result of the electron diffraction pattern inset in Fig. 7(a), the relative orientation of the  $\alpha$  and  $\beta$  phases satisfied the following relationship:  $\{0001\}_{\alpha}/\langle 110\rangle_{\beta}, \langle 1120\rangle_{\alpha}/\langle 111\rangle_{\beta}$  [29].

The TEM of specimen 2 in Fig. 7(b) reveals that the  $\beta/B2$  phase (dark laths) without allotropic transformation remained between  $\alpha_2$  laths. As the content of TiAl increases, based on Table 2, Al, Nb, and Cr content gradually increasing, while V and Ti content gradually decreased. When the local Al concentration exceeded the critical value, ordering transformation from  $\alpha$  to  $\alpha_2$  can be promoted [30]. The measured result of the electron diffraction pattern inset in Fig. 7(b) displayed superlattice spots, which was indicative of the formation of ordered  $\alpha_2$  phase. The TEM of specimen 3 in Fig. 7(c) revealed that the B2 and  $\gamma$  phases existed between  $\alpha_2$  laths. Normally, excessive Al could ascribe to segregate along and within laths and promote  $\alpha_2 \rightarrow \gamma$  phase transformation. The nucleation and growth of B2 and  $\gamma$  phases between  $\alpha_2$  laths could be observed in Fig. 7(c), which were identical to the results in Fig. 5(c). During the dissolution of lath-shaped  $\alpha_2$  and precipitation of blocky  $\gamma$ , it often occurred with the appearing of dislocation in the contiguous  $\gamma$ , according to Fig. 7(d). This attributed to the rapid heating and cooling during LMD, which results in a comparatively high thermal stress between the  $\alpha_2$  and  $\gamma$  owing to their large differences in expansion coefficient and elastic modulus. [32].

Moreover, the high temperature in LMD can notably accelerate the diffusion of elements [33]. As  $\alpha$  stabilizing element, Al atoms diffused into the  $\alpha$  region, while V, Nb, and Cr diffused into the  $\beta$  region as  $\beta$  stabilizing element [31]. Moreover, Nb and Cr elements, as  $\beta$  stabilizing elements, can extend the  $\beta$  phase region and prevent the transition of  $\beta$  by reducing the allotropic transformation temperature, which can be confirmed by the content of  $\beta/B2$  in Fig. 5 and TEM results in Fig. 7. There are three different formation mechanisms for the B2 phase. The first one is  $\beta \rightarrow B2$ , the formation of the B2 phase was the result of the ordering transformation by residual  $\beta$  phase. Hence controlling the process of richening Nb can prevent the forming of B2 phase. Second, the B2 phase directly precipitated and grew within lath-shaped  $\alpha_2$  by

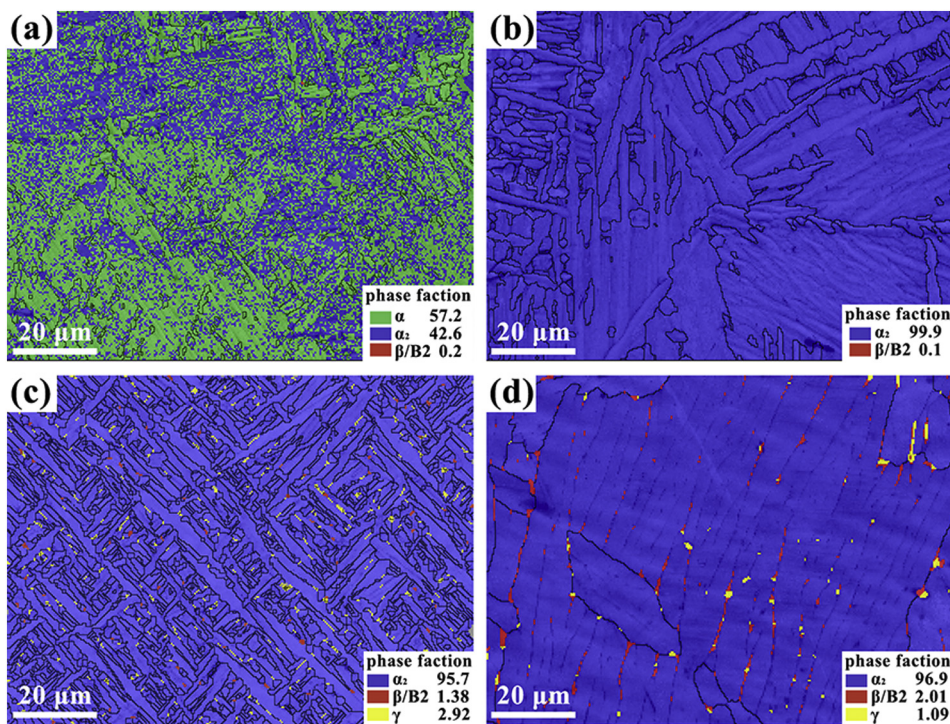


**Fig. 5.** EBSD combination map of phase distributions, band contrast, and grain boundaries (black lines) of as-deposited LMD alloys: (a) specimen 1; (b) specimen 2; (c) specimen 3; (d) specimen 4.

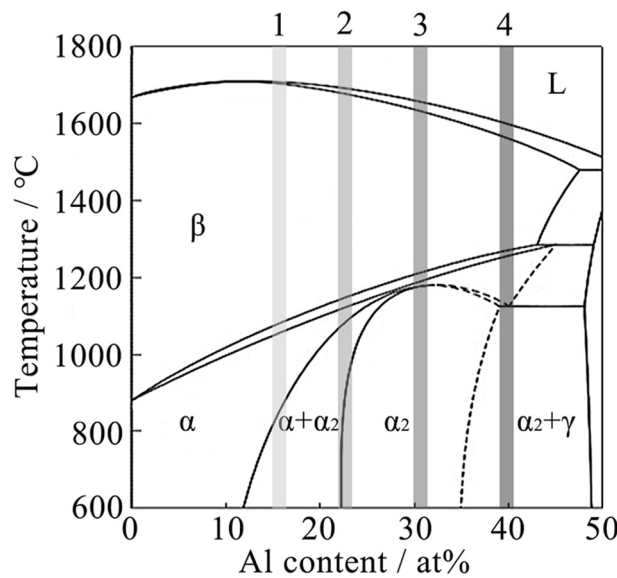


**Fig. 6.** Ti-Al phase diagram.

the transformation of  $\alpha_2 \rightarrow \text{B2}$  [34]. Third, the B2 phase could also form by the eutectoid reaction of  $\alpha_2 + \gamma \rightarrow \text{B2}$  and grow to situate  $\alpha_2/\gamma$  interface by consuming  $\alpha_2$  and  $\gamma$  phases [35].

#### 3.4. Tensile properties and fracture mechanism

The tensile properties of the specimen 1, specimen 2, specimen 3 and specimen 4 at room temperature (RT), 650 °C, and 750 °C are shown in Fig. 8. In the tensile properties testing, three parallel-samples were set for each condition. Fig. 8 shows the average values under each condition. At RT, increasing the TiAl content could gradually reduce the tensile properties, a significant loss of the ultimate tensile strength (UTS) from 1083 MPa to 317 MPa and elongation from 4.6% to 0.8%

were observed. Therefore the specimen 1 attained the highest UTS (1083 MPa) and elongation (4.60%). At 650 °C and 750 °C, with the increasing of TiAl content, the UTS of alloys showed a trend of increasing first and then decreasing, while the elongation gradually decreased. The UTS of specimen 3 attained maximum values, which were 572 MPa and 562 MPa, respectively. Therefore, for TC4-TiAl alloy, it's better that the addition of TiAl is about 20% when working at room temperature, and about 60% when working at 650–750 °C.

To clearly define the fracture mechanism, the fracture morphologies of specimens under RT, 650 °C and 750 °C were observed in Figs. 9, 10, and 11, respectively. At RT, the fracture morphologies of specimen 1, specimen 2, specimen 3, and specimen 4 composed of tearing ridges and cleavage planes. With the increase of TiAl content, the tearing edge decreased, while the cleavage planes increased, indicating that the plasticity reduced. Hence, the fractured mode of specimen 1, specimen 2, specimen 3, and specimen 4 under RT belonged to quasi-cleavage fracture. At 650 °C, large quantity dimples with uniform size and greater depth were presented in Fig. 10(a) revealing a ductile fracture in specimen 1. For specimen 2, dimples shown in Fig. 10(b) were shallower, accompanying with the formation of a few short tearing ridges between dimples. The dimples disappeared and fracture morphology of specimen 3 was covered with curved tearing ridges and a small number of cleavage planes. As shown in Fig. 10(d), the tearing ridges became longer and straighter, and the number and size of cleavage planes also increased. Based on the phenomenon above, at 650 °C, the fracture mechanism of specimen 1 and specimen 2 revealed a ductile fracture feature, while specimen 3 and specimen 4 belonged to quasi-cleavage fracture. At 750 °C, fracture morphologies of specimen 1, specimen 2, and specimen 3 were covered with dimples (see Fig. 11(a)–(c)), which was indicative of the ductile fracture. With the increase of TiAl content, the number and size of the dimples decreased, indicating the drop of plasticity, which was consistent with the experimental results in Fig. 8. The fracture morphology of specimen 4 (see Fig. 11(d)) tested at 750 °C was covered with a lot of tearing ridges and cleavage planes, which was indicative of quasi-cleavage fracture.

Normally, grain size, phase constituents, and microstructure

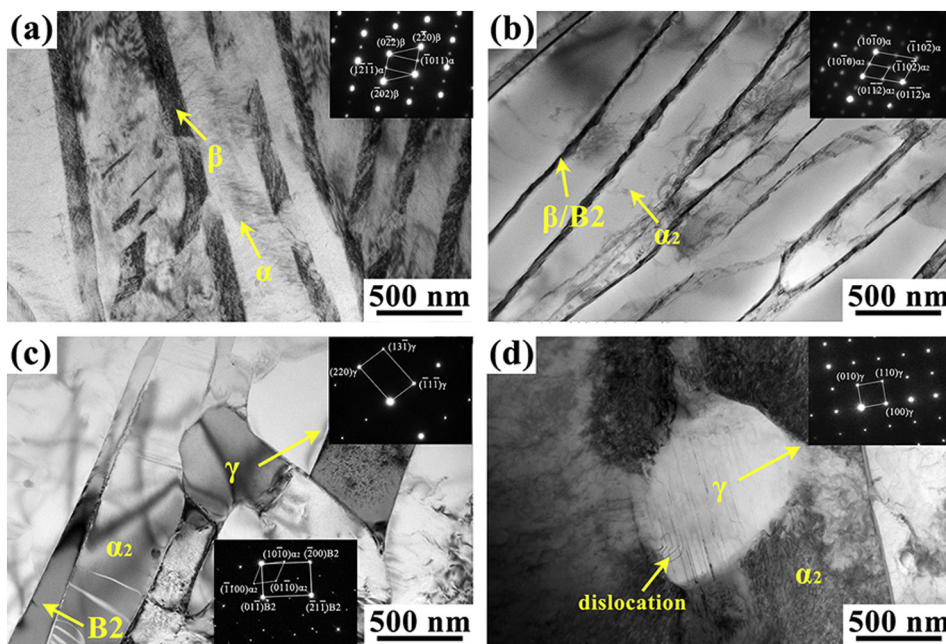


Fig. 7. TEM images of microstructure morphology of the as-deposited LMD alloys: (a) specimen 1; (b) specimen 2; (c) specimen 3; (d) specimen 4.

**Table 2**  
The chemical composition of the as-deposited LMD alloys (at.-%).

	Ti	Al	V	Nb	Cr
Specimen 1	81.69	14.35	3.18	0.41	0.37
Specimen 2	73.37	22.71	2.37	0.79	0.76
Specimen 3	64.92	31.12	1.55	1.28	1.13
Specimen 4	56.56	39.48	0.77	1.65	1.54

uniformity have significant effects on tensile properties [36–38]. As we all know, solid solutions have better plasticity than intermetallic compounds. Due to the small difference in electronegativity between the solute and the solvent in the solid solution, atoms are bonded by metallic bonds. Thus dislocations can bypass the precipitate phases, occurring to plastic deformation. However, for the intermetallic compounds, the large difference in electronegativity gives rise to form ionic bonds with high strength, which dislocations require a large amount of energy to move. Moreover, it is noteworthy that cracks might be more inclined to appear and propagate along with intermetallic compounds, because of the relatively weak bonding force among intermetallic resulting from the much higher hardness of intermetallic [39]. Therefore, the intermetallic compound exhibits strong brittleness and thermal

stability. The decreased ductility with increasing Al content was caused by the increased ionic bonds or decreased metallic bonds [40–42]. On the basis of the theory above, in this study, the UTS and elongation of specimen 1 at RT were the highest on account of the presence of solid solution  $\alpha$ . Furthermore, the presence of  $\alpha_2$  and  $\gamma$  intermetallic compounds could reduce strength and plasticity at RT, but, at the same time, increase the thermal stability of the alloy [43]. As the temperature rose, the softening of the  $\alpha$  phase could lead to a decrease in the strength and a prominent increase in the plasticity of specimen 1 at 650 °C and 750 °C. Besides, the high-temperature UTS of specimen 3 were better than that of other specimens for the following three reasons: on the one hand, grain sizes are of prime importance in mechanical properties. The uniform and compact laths of specimen 3 were thinner than that of other specimens as shown in Fig. 3, which might lead to fine-grain strengthening. On the other hand, the  $\gamma$  phase and the  $\beta/B2$  phase in specimen 3 which were small in size and uniformly distributed between the  $\alpha_2$  laths had the effect of dispersion strengthening. Furthermore, compared with other specimens shown in Fig. 5, the  $\gamma$  phase had the largest content in specimen 3, which was more stable than the  $\alpha_2$  phase at high-temperature. However, due to the formation of the coarsening of  $\alpha_2$  lamellar as well as the obvious aggregation and growth of the  $\gamma$  phase and  $\beta/B2$  phase, tensile properties

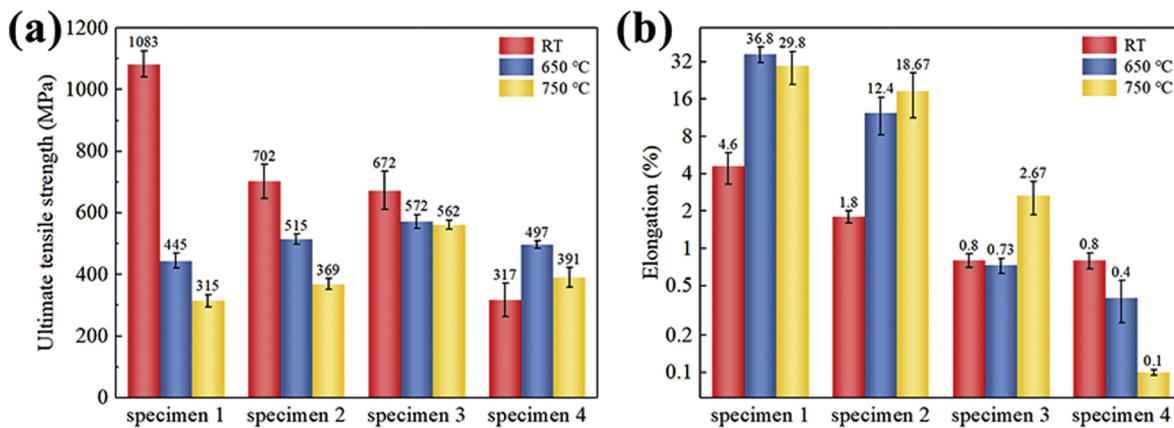
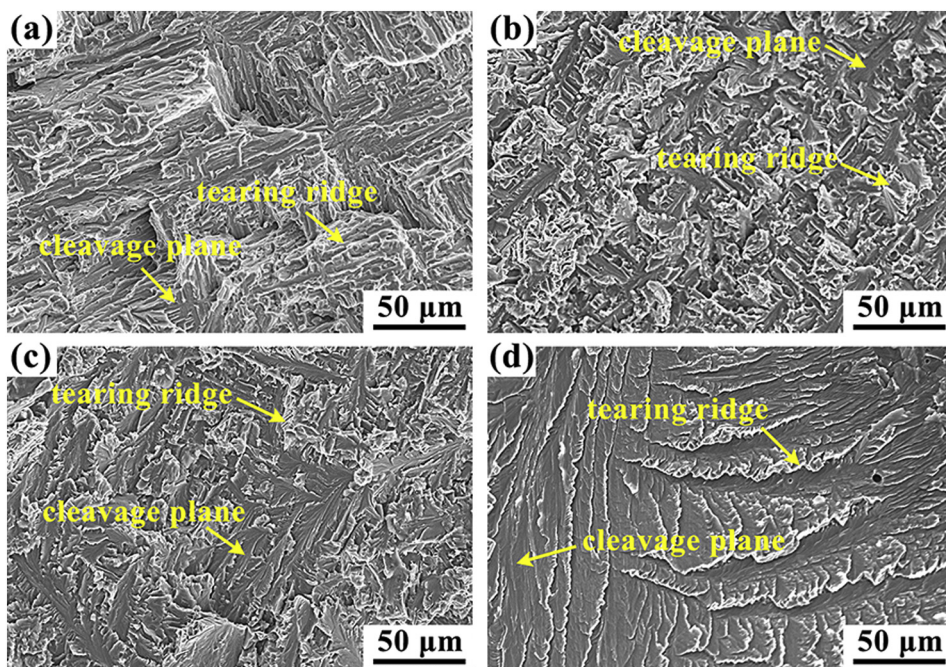


Fig. 8. Tensile properties of the as-deposited LMD alloys: (a) ultimate tensile strength; (b) elongation.



**Fig. 9.** Fracture morphologies of the as-deposited LMD alloys under RT: (a) specimen 1; (b) specimen 2; (c) specimen 3; (d) specimen 4.

of specimen 4 at all temperatures tested in this work were relatively poor. Hence, the order of the thermal stability, determined based on the tensile test results for RT, 650 °C and 750 °C, was  $\gamma > \alpha_2 > \alpha$ . Obviously, further work is demanded to adjust relevant process parameters to controlling of lamellar width and B2 phase content, which should refine grains and improve component properties fabricated by LMD.

#### 4. Conclusions

In this paper, the TC4-xTiAl ( $x = 20\%, 40\%, 60\%, 80\%$  wt%) specimens were successfully fabricated by LMD from mixtures of TC4/

TiAl powders. The main conclusions are summarized as follows:

- (1) As TiAl content increased, the microstructure gradually transformed from basket weave structure to lamellar structure, accompanying with the formation of  $\alpha_2$ ,  $\gamma$ , and B2 phases. The addition of TiAl increased the content of Al, Nb, Cr. When the local Al concentration exceeds a critical value, the phase transformations of  $\alpha \rightarrow \alpha_2$  and  $\alpha_2 \rightarrow \gamma$  can be promoted. Nb and Cr elements, as  $\beta$ -stabilizing elements, can decrease the allotropic transformation temperature, extend the  $\beta$  phase region and prevent the transition of  $\beta$ . The above two reasons result in the precipitation of  $\alpha_2$ ,  $\beta$ /B2 phases.

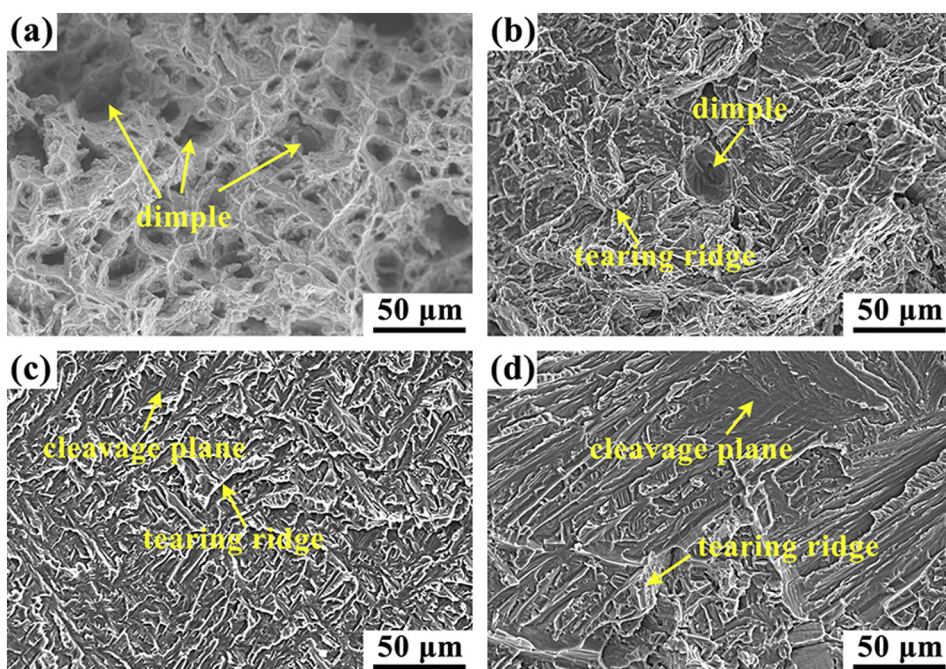


**Fig. 10.** Fracture morphologies of the as-deposited LMD alloys under 650 °C: (a) specimen 1; (b) specimen 2; (c) specimen 3; (d) specimen 4.

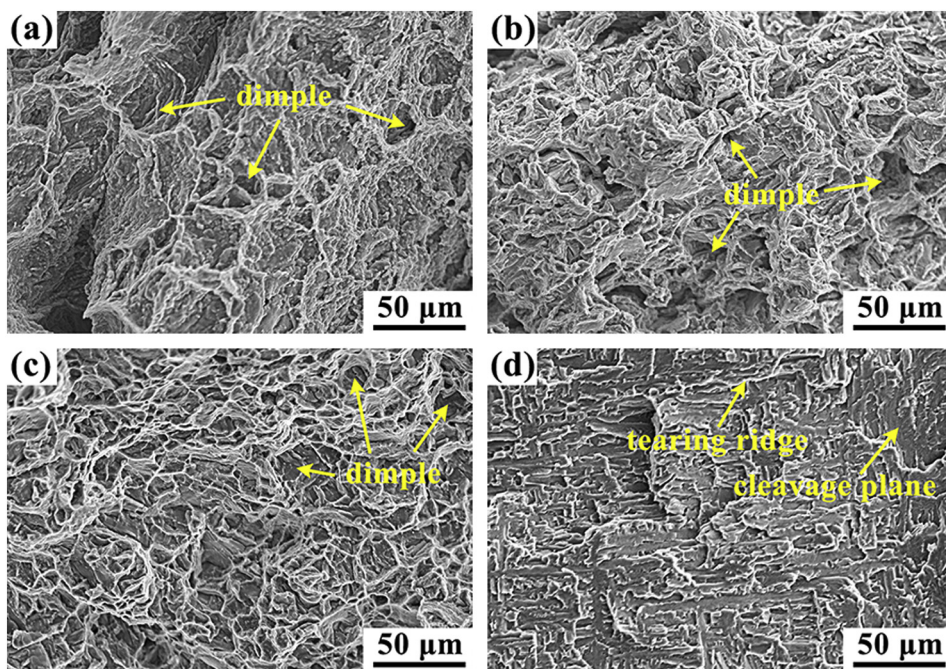


**Fig. 11.** Fracture morphologies of the as-deposited LMD alloys under 750 °C: (a) specimen 1; (b) specimen 2; (c) specimen 3; (d) specimen 4.

- (2) At RT, the addition of TiAl led to a decrease of the tensile properties, the specimen 1 (TC4-20%TiAl) had the highest UTS (1083 MPa) and elongation (4.60%) due to the presence of solid solution  $\alpha$ . At 650 °C and 750 °C, the UTS of specimen 3 (TC4-60%TiAl) had the maximum values, which were 572 MPa and 562 MPa, respectively, attributing to the presence highest content of  $\gamma$  phase and the dispersion strengthening ascribed by the small size  $\gamma$  phase and the B2 phase.
- (3) The tensile properties at room and high temperatures are strongly dependent on phase composition. At RT, the solid solution  $\alpha$  phase had better plasticity compared with intermetallic compound. The formations of the intermetallic compound  $\alpha_2$  and  $\gamma$  reduce the strength and plasticity of the alloys at room temperature and, meanwhile, increase the thermal stability. In particular,  $\gamma$  is more stable than  $\alpha_2$  at high-temperature.

#### Declaration of competing interest

The authors declare that they have no known competing financial interests or personal relationships that could have appeared to influence the work reported in this paper.

#### Acknowledgements

The work was financially supported by the National Key Research and Development Program of China (Grant No. 2017YFB1103600).

#### Data availability

The raw/processed data required to reproduce these findings cannot be shared at this time as the data also forms part of an ongoing study.

#### References

- [1] T. Wang, Y.Y. Zhu, S.Q. Zhang, H.B. Tang, H.M. Wang, Grain morphology evolution behavior of titanium alloy components during laser melting deposition additive manufacturing, *J. Alloys Compd.* 632 (2015) 505–513.
- [2] J. Li, H.M. Wang, Microstructure and mechanical properties of rapid directionally solidified Ni-base superalloy Rene'41 by laser melting deposition manufacturing, *Mater. Sci. Eng. A* 527 (2010) 4823–4829.
- [3] Y. Zhai, D.A. Lados, J.L. LaGoy, Additive manufacturing: making imagination the major limitation, *Jom* 66 (2014) 808–816.
- [4] H.P. Qu, H.M. Wang, Microstructure and mechanical properties of laser melting deposited  $\gamma$ -TiAl intermetallic alloys, *Mater. Sci. Eng. A* 466 (2007) 187–194.
- [5] B. Heer, A. Bandyopadhyay, Compositionally graded magnetic-nonnagnetic bimetallic structure using laser engineered net shaping, *Mater. Lett.* 216 (2018) 16–19.
- [6] X. Lin, T.M. Yue, H.O. Yang, W.D. Huang, Laser rapid forming of SS316L/Rene88DT graded material, *Mater. Sci. Eng. A* 391 (2005) 325–336.
- [7] Y. Wang, R. Chen, X. Cheng, Y. Zhu, J. Zhang, H. Wang, Effects of microstructure on fatigue crack propagation behavior in a bi-modal TC11 titanium alloy fabricated via laser additive manufacturing, *Journal of Materials Science & Technology* 35 (2019) 403–408.
- [8] Q. Zhang, J. Chen, H. Tan, X. Lin, W.-d. Huang, Microstructure evolution and mechanical properties of laser additive manufactured Ti-5Al-2Sn-2Zr-4Mo-4Cr alloy, *Trans. Nonferrous Metals Soc. China* 26 (2016) 2058–2066.
- [9] Y. Zhai, D.A. Lados, E.J. Brown, G.N. Vigilante, Understanding the microstructure and mechanical properties of Ti-6Al-4V and Inconel 718 alloys manufactured by laser engineered net shaping, *Additive Manufacturing* 27 (2019) 334–344.
- [10] R. Sabban, S. Bahl, K. Chatterjee, S. Suwas, Globalization using heat treatment in additively manufactured Ti-6Al-4V for high strength and toughness, *Acta Mater.* 162 (2019) 239–254.
- [11] S. Liu, Y.C. Shin, Additive manufacturing of Ti6Al4V alloy: a review, *Mater. Des.* 164 (2019).
- [12] H.S. Ren, D. Liu, H.B. Tang, X.J. Tian, Y.Y. Zhu, H.M. Wang, Microstructure and mechanical properties of a graded structural material, *Mater. Sci. Eng. A* 611 (2014) 362–369.
- [13] W. Meng, Y. Xiaohui, W. Zhang, F. Junfei, G. Lijie, M. Qunshuang, C. Bing, Additive manufacturing of a functionally graded material from Inconel625 to Ti6Al4V by laser synchronous preheating, *J. Mater. Process. Technol.* 275 (2020) 116368.
- [14] W. Chen, Z. Li, Additive manufacturing of titanium aluminides, *Additive Manufacturing for the Aerospace Industry*, 2019, pp. 235–263.
- [15] H.P. Qu, P. Li, S.Q. Zhang, A. Li, H.M. Wang, The effects of heat treatment on the microstructure and mechanical property of laser melting deposition  $\gamma$ -TiAl intermetallic alloys, *Mater. Des.* 31 (2010) 2201–2210.
- [16] H.P. Qu, P. Li, S.Q. Zhang, A. Li, H.M. Wang, Microstructure and mechanical property of laser melting deposition (LMD) Ti/TiAl structural gradient material, *Mater. Des.* 31 (2010) 574–582.
- [17] Y.-J. Liang, X.-J. Tian, Y.-Y. Zhu, J. Li, H.-M. Wang, Compositional variation and microstructural evolution in laser additive manufactured Ti/Ti-6Al-2Zr-1Mo-1V graded structural material, *Mater. Sci. Eng. A* 599 (2014) 242–246.
- [18] Y. Liu, C. Liang, W. Liu, Y. Ma, C. Liu, C. Zhang, Dilution of Al and V through laser powder deposition enables a continuously compositionally Ti/Ti6Al4V graded structure, *J. Alloys Compd.* 763 (2018) 376–383.
- [19] C. Shang, C. Wang, G. Xu, C. Li, J. You, Laser additive manufacturing of TA15 - Inconel 718 bimetallic structure via Nb/Cu multi-interlayer, *Vacuum* 169 (2019).
- [20] Y. Wu, X. Cheng, S. Zhang, D. Liu, H. Wang, Microstructure and phase evolution in  $\gamma$ -TiAl/Ti2AlNb dual alloy fabricated by direct metal deposition, *Intermetallics* 106 (2019) 26–35.
- [21] M.S. Domack, J.M. Baughman, Development of nickel-titanium graded composition components, *Rapid Prototyp. J.* 11 (2005) 41–51.

- [22] J. Zhang, Y. Wu, X. Cheng, S. Zhang, H. Wang, Study of microstructure evolution and preference growth direction in a fully laminated directional micro-columnar TiAl fabricated using laser additive manufacturing technique, *Mater. Lett.* 243 (2019) 62–65.
- [23] C. Tan, K. Zhou, T. Kuang, Selective laser melting of tungsten-copper functionally graded material, *Mater. Lett.* 237 (2019) 328–331.
- [24] C. Shang, G. Xu, C. Wang, G. Yang, J. You, Laser deposition manufacturing of bimetallic structure from TA15 to inconel 718 via copper interlayer, *Mater. Lett.* 252 (2019) 342–344.
- [25] W.J. Zhang, X.Y. Song, S.X. Hui, W.J. Ye, Y.L. Wang, W.Q. Wang, Tensile behavior at 700 °C in Ti-Al-Sn-Zr-Mo-Nb-W-Si alloy with a bi-modal microstructure, *Mater. Sci. Eng. A* 595 (2014) 159–164.
- [26] P.L. Narayana, S.-W. Kim, J.-K. Hong, N.S. Reddy, J.-T. Yeom, Tensile properties of a newly developed high-temperature titanium alloy at room temperature and 650 °C, *Mater. Sci. Eng. A* 718 (2018) 287–291.
- [27] X. Ding, L. Zhang, J. He, F. Zhang, X. Feng, H. Nan, J. Lin, Y.-W. Kim, As-cast microstructure characteristics dependent on solidification mode in TiAl-Nb alloys, *J. Alloys Compd.* 809 (2019) 151862.
- [28] S.H. Kim, H.K. Moon, T. Kang, C.S. Lee, Dissolution kinetics of delta ferrite in AISI 304 stainless steel produced by strip casting process, *Mater. Sci. Eng. A* 356 (2003) 390–398.
- [29] P. Kumar, U. Ramamurty, Microstructural optimization through heat treatment for enhancing the fracture toughness and fatigue crack growth resistance of selective laser melted Ti 6Al 4V alloy, *Acta Mater.* 169 (2019) 45–59.
- [30] H. Wu, G. Fan, L. Geng, X. Cui, M. Huang, Nanoscale origins of the oriented precipitation of Ti3Al in Ti Al systems, *Scr. Mater.* 125 (2016) 34–38.
- [31] G.L. Chen, X.J. Xu, Z.K. Teng, Y.L. Wang, J.P. Lin, Microsegregation in high Nb containing TiAl alloy ingots beyond laboratory scale, *Intermetallics* 15 (2007) 625–631.
- [32] F. Appel, U. Lorenz, M. Oehring, U. Sparka, R.J.M.S. Wagner, E. A, Thermally activated deformation mechanisms in micro-alloyed two-phase titanium amminide alloys, *Materials Science & Engineering A* 233 (1997) 1–14.
- [33] X. Cui, S. Zhang, C. Wang, C.H. Zhang, J. Chen, J.B. Zhang, Microstructure and fatigue behavior of a laser additive manufactured 12CrNi2 low alloy steel, *Mater. Sci. Eng. A* 772 (2019) 138685.
- [34] Z.W. Huang, W. Voce, P.J.S.M. Bowen, Thermal exposure induced  $\alpha_2 + \gamma \rightarrow B2(\omega)$  and  $\alpha_2 \rightarrow B2(\omega)$  phase transformations in a high Nb fully lamellar TiAl alloy, *Ser. Mater.* 48 (2003) 79–84.
- [35] J. Beddoes, W.R. Chen, L. Zhao, Precipitation of particles in a fully lamellar Ti-47Al-2Nb-1Mn-0.5W-0.5Mo-0.2Si (at.%) alloy, *Journal of Materials Ence* 37 (2002) 621–627.
- [36] X. Liang, Y. Liu, H. Li, Z. Gan, B. Liu, Y. He, An investigation on microstructural and mechanical properties of powder metallurgical TiAl alloy during hot pack-rolling, *Mater. Sci. Eng. A* 619 (2014) 265–273.
- [37] Z.W. Huang, J.P. Lin, Z.X. Zhao, H.L. Sun, Fatigue response of a grain refined TiAl alloy Ti-44Al-5Nb-1W-1B with varied surface quality and thermal exposure history, *Intermetallics* 85 (2017) 1–14.
- [38] H. Zhou, F. Kong, K. Wu, X. Wang, Y. Chen, Hot pack rolling nearly lamellar Ti-44Al-8Nb-(W, B, Y) alloy with different rolling reductions: lamellar colonies evolution and tensile properties, *Mater. Des.* 121 (2017) 202–212.
- [39] J. Li, S. Qiao, D. Han, M. Li, Damage behaviors of TiAl alloy under thermal fatigue and thermal cycling with dead-load, *Mater. Sci. Eng. A* 471 (2007) 106–112.
- [40] Y.-W. K., M. Dennis, Progress in the understanding of gamma titanium Aluminides, *JOM: The Journal of the Minerals, Metals & Materials Society* 43 (1991) 40–47.
- [41] H. Wu, L. Geng, G. Fan, X. Teng, H. Qi, Nanoscale strain characterization of Ti3Al precipitate-reinforced Ti alloys, *Mater. Lett.* 209 (2017) 182–184.
- [42] L. Bolzoni, S. Raynova, F. Yang, Strengthening mechanisms of Ti via Al addition, *J. Alloys Compd.* 820 (2020) 153447.
- [43] A. Madsen, H. Ghonem, Effects of aging on the tensile and fatigue behavior of the near- $\alpha$  Ti-1100 at room temperature and 593 °C, *Mater. Sci. Eng. A* 177 (1994) 63–73.